ELSEVIER

Thin Solid Films 406 (2002) 151–158

thin solid films

www.elsevier.com/locate/tsf

Correlation between bulk morphology and luminescence in porous silicon investigated by pore collapse resulting from drying

Michael D. Mason, Donald J. Sirbuly, Steven K. Buratto*

Department of Chemistry and Biochemistry, University of California, Santa Barbara, CA 93106-9510, USA

Received 1 June 2001; received in revised form 20 November 2001; accepted 11 December 2001

Abstract

We used a combination of scanning electron microscopy, laser scanning confocal microscopy and luminescence spectroscopy to correlate the emission properties of anodized porous silicon (PS) with film morphology in samples that have undergone solvent evaporation-induced collapse of the underlying porous structure. Several PS samples were investigated as a function of the current density (J) and total etch time, while the total charge (Q) injected per unit area (with the total amount of Si removed) was kept constant during etching. From these data, two classes of PS samples emerge. Porous silicon samples produced at high current density have a three-dimensional pore network with a narrow distribution of blue–green emitting chromophores. In contrast, low current density samples form a two-dimensional pore network normal to the Si substrate with larger chromophores and exhibit broad red luminescence.

Keywords: Electrochemistry; Fluorescence; Scanning electron microscopy; Silicon

1. Introduction

Visible light emission from Si via anodic etching in aqueous HF, called porous silicon (PS), has stimulated tremendous interest over the past several years due to its potential application in opto-electronic devices, such as light emitting diodes (LEDs) and lasers and the ability to be integrated with current Si processing technology [1,2]. To date, much of the research on PS has been devoted to developing a detailed understanding of the emission mechanism, which has been attributed primarily to an excited state confinement effect [3]. Although a quantum confinement model for the light emission mechanism of as-prepared porous silicon has gained widespread support, the high degree of structural inhomogeneity and parametric tunability of etched samples have made a direct correlation between chromophore size and optical bandgap difficult.

In most cases, the 'diameter' of the silicon framework within the layer is estimated as a linear function of sample porosity. Support for this conclusion is drawn from a host of fluorescence data, specifically a shift towards higher emission energies with an increase in exposure to the electrolyte, an increase in current density, or an increase in HF concentration.

In previous studies, sample porosities have been almost exclusively determined using a combination of gravimetric and microscopy techniques. In one case, the volume and mass of the porous silicon are determined by first removing the porous layer by means of a very short high current etch period (free standing PS), which is then weighed and its thickness measured directly [4]. In a second technique, the entire porous silicon layer is etched away by additional exposure to a strong acid leaving a circular 'pit', the volume of which is determined by conventional far-field optical microscopy, and the mass is determined by differential mass analysis [5]. While these techniques provide useful information about the mass and volume of the porous silicon layer, and even the amount of free space within the layer, they do not address how the remaining silicon is distributed within the sample. In fact, in situ HRTEM cross-sectional micrographs by different groups have shown either a branched tree-like structure or a vertical columnar structure, both having a broad range of Si chromophore sizes [6–8]. Similar images of free-standing

*Corresponding author. Tel.: +1-805-893-3393.
E-mail address: buratto@chem.ucsb.edu (S.K. Buratto).

0040-6090/02/$ - see front matter
PII: S0040-6090(01)01776-X

porous silicon have suggested a more web-like structure, showing a narrower chromophore size distribution [9]. If we wish to discuss the emission properties of PS in the context of a quantum confinement model, then it is of critical importance to understand how the sizes of the in situ chromophores are related to the preparation conditions.

One common characteristic of as-prepared porous silicon is its tendency to deform and crack during drying. While this is generally undesirable in terms of the mechanical stability and device type applications, the particular morphologies that are produced during solvent evaporation provide an insight into the geometry of the pore structure and PS network of the in situ sample. In this study, PS samples were prepared by carefully controlling the total charge supplied during etching. In this way, samples with the same pore volume were made, under different etch parameters, and their resultant morphologies after drying were compared. Scanning electron microscopy (SEM) was used to directly image the sample structure, while laser scanning confocal microscopy (LSCM) and fluorescence microscopy were used to correlate the structure with emission and spectroscopic properties. A multi-dimensional evaporation induced pore collapse model was used to describe the observed morphologies and corresponding emission data. This work provides further evidence of a series of cylindrical two-dimensional pores, in the case of low current density PS, and a three-dimensional pore network in the case of higher current density PS samples [10,11]. In addition, the pore geometry and spectral distribution (chromophore size) are strongly dependent on the current used for etching, but only weakly dependent on the etch time.

2. Experimental

Porous silicon samples were fabricated by anodically etching p-type (boron doped) silicon wafers, with a resistivity of $\sim 5\ \Omega$ cm, normal to the (100) surface in 15% HF/ethanol solutions. The electrochemical cell used for fabrication is similar to that used by Sailor et al. [12], consisting of a Teflon electrolyte holder, cylindrical aluminum electrode and a Pt working electrode. A uniform and reproducible back-side electrical contact was made by imbedding a GaIn eutectic between the Si wafer and the cylindrical aluminum electrode. Anodization times of 5–60 min with constant current densities ranging from 3 to 35 mA/cm^2 were used to prepare the samples. Etched samples were rinsed in ethanol, dried rapidly under a steady stream of nitrogen, and stored under vacuum (>24 h) to slow the aging process of the hydrogen-terminated PS samples and to ensure dryness.

Cross-sections were prepared for electron microscopy by inscribing the back-side of the sample and carefully fracturing the (100) plane through the center of the etched region. The samples were carbon-coated to reduce the accumulation of charge on the PS surface during scanning, improving image contrast. SEM images were acquired using a JEOL 630OF microscope. Acceleration voltage was kept at 3–5 kV and sample-to-gun distances were between 8 and 25 mm. The extract current was monitored and kept between 6.5 and 8 μA. SEM images were captured while scanning the electron beam at an angle of 30° relative to the Si substrate, providing both cross-section and spatial information.

The thickness of the porous silicon was determined by direct analysis of the SEM images. While the specific geometry of our electrochemical cell produces nearly homogeneous samples, inhomogeneities do exist near the edges of the etch region. For this reason, only the central 60% of the sample was used, where the thickness varies by only 3–5%. To ensure accurate results, samples were reproduced under each set of etch conditions, and 8–10 points were measured on each sample.

Sequential fluorescence images were obtained during drying using a Leitz fluorescent microscope (Leica Microsystems) coupled to a CCD camera (Santa Barbara Instrument Group). The illumination source was the 400–490 nm portion of a xenon arc lamp, separated using a filter cube, which was focussed onto the sample with a $10\times$ air objective (NA = 0.40). Emission spectra (0.25 s integration) were acquired using the same instrument. Fluorescence was collected into an optical fiber and directed to the entrance slit of a 0.25 m monochromator (ARC Inc.), coupled to the same CCD camera mentioned above.

High spatial resolution fluorescence images were obtained using a laser scanning confocal microscope (LCSM), described in detail elsewhere [13]. The 457 nm line of an argon ion laser (Spectra Physics), attenuated to approximately 5 μW and circularly polarized, was focussed to a near diffraction limited spot (~ 350 nm) using a 1.25 NA air objective. The sample emission was collected using the same objective and passed through a holographic notch filter (Kaiser Optical) to isolate the scattered laser light from the fluorescence emission which was then directed to an avalanche photodiode (APD) single photon counting module (EG and G). Fluorescence images were acquired by raster scanning the samples on a four-quadrant piezo tube (Stavely Sensors) controlled by commercial scanning electronics (Digital Instruments). Fluorescence spectra were also collected using this apparatus by re-directing the emission into a fiber coupler attached to a CCD spectrometer. Spectra obtained using this microscope showed similar lineshapes and spectral positions to the ones (Fig. 2) captured by the fluorescent microscope described earlier.

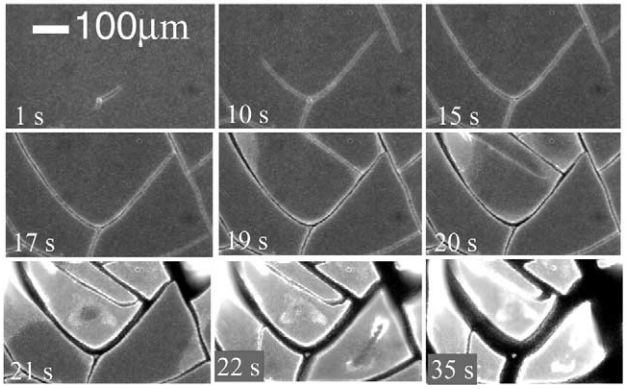

Fig. 1. Sequential 350×570 μm wide-field luminescence images of a 12 mA/10 min PS sample during drying. The elapsed time for each image is shown on the bottom left and the integration time was 0.5 s. Each image is shown on the same linear gray-scale.

3. Results and discussion

In Fig. 1, a series of 350×575 μm wide-field fluorescence images, acquired during solvent evaporation, are shown for a thin sample prepared under high current density ($J=12$ mA/cm^2). These images exhibit fluorescence morphology behavior representative of all of the high current density samples discussed here, and are similar to those previously reported [10,14]. The first image in the series (Fig. 1, 1 s) exhibits nearly uniform fluorescence with only a single small crack feature beginning to form as the solvent front reaches the surface of the porous silicon.

Here, the pore dimensions are well below the resolution limit of the microscope and are, therefore, not directly observed. As evaporation proceeds, the cracks clearly propagate across the sample forming isolated regions or 'platelets', leaving the non-luminescent silicon substrate exposed as black regions in last image. The total integrated intensity of the still-wet porous silicon (1 s image) is approximately half that of the dried sample (120 s image). This increase in the fluorescence intensity might be understood simply as a result of solvent quenching, which has been shown to dramatically decrease the luminescence of porous silicon [15]. The edges of the crack features, however, appear bright relative to the interior of the platelets, regardless of whether the sample is dry or not.

There are several possible explanations for this behavior. First, because these images were acquired using a wide-field, long working distance objective, the curling of the platelet away from the substrate may bring the edges into a plane of higher excitation density, resulting in an increase in fluorescence. This was readily ruled out in our experiments by adjusting the focal plane of the microscope objective (the depth-of-focus for the objective used was ~0.5 μm), which had little effect on the relative intensities of the features discussed here.

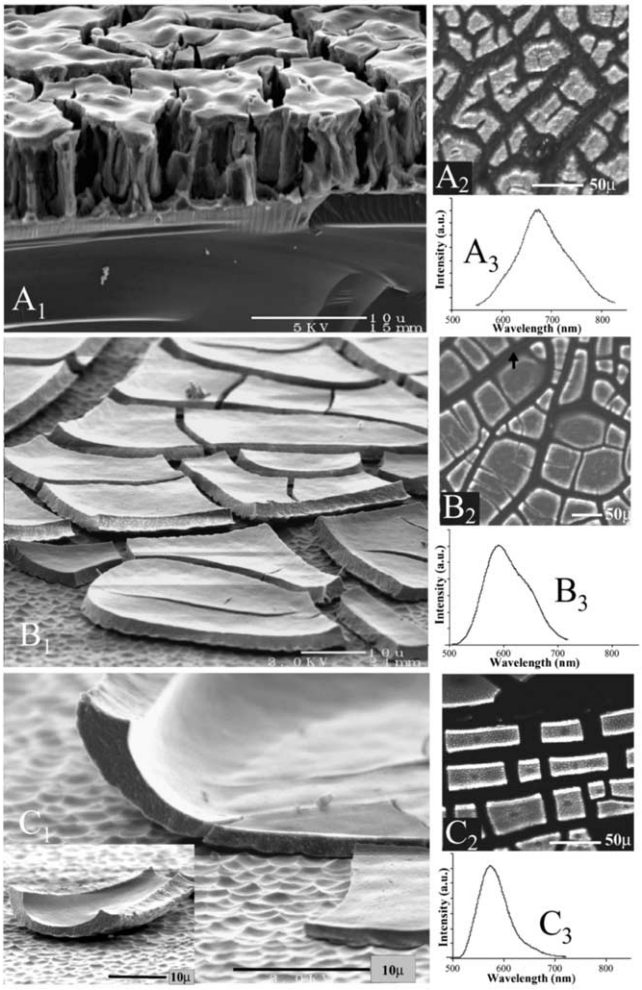

Fig. 2. Porous Si morphology and luminescence as a function of etching current density. The total charge ($Q=6000$ mC/cm^2) is kept constant for each of the three samples. Three different current densities are shown: low current density (5 mA/cm^2) shown in part (A), moderate current density (10 mA/cm^2) shown in part (B), and high current density (15 mA/cm^2), shown in part (C). The morphology of each sample is shown in the electron micrographs A_1, B_1 and C_1. The corresponding luminescence micrograph for each sample is shown in A_2, B_2 and C_2. Representative luminescence spectra are shown in A_3, B_3 and C_3, respectively.

Secondly, for relatively thin samples, as shown here, the energy transfer from the porous silicon into the Si substrate may be possible in regions where curling has not occurred and the PS–Si interface is intact. Since the bulk Si is not luminescent, this process results in a dark spot. Finally, the spatial density of chromophores (and non-fluorescent scattering centers) or the absorption cross-section may vary across each platelet as a result of the pore collapse. In the still-wet as-prepared sample, we can assume that the spatial density of chromophores is approximately uniform, as seen from the uniformity of the fluorescence images (Fig. 1, 1s). In the dried sample the thickness across a single platelet can vary by a factor of two from edge-to-middle (Fig. 2C_1 —

inset); therefore, it must be the case that the density of chromophores has increased (or decreased). It seems clear from these data that the observed optical properties are dependent on the local nanoscale morphology of the rapidly dried samples. In order to sort out this dependence, a more detailed investigation of the relationship between the observed optical and morphological properties, for a variety of etching conditions, is required.

By adjusting the etching time and current density of the electrochemical process a wide range of porous silicon morphologies were produced as seen in the scanning electron microscopic images ($2A_1$, $2B_1$ and $2C_1$) in Fig. 2. In order to investigate the relationship between etch conditions and pore geometry, it is necessary to prepare samples in which the total amount of silicon removed is constant. As with all electrochemical processes, the extent of the reaction can be quantitatively controlled as a function of the total number of charges injected into the system. While the dissolution mechanism of porous silicon is still widely debated, the effective dissolution valence under the etching conditions discussed here is 2, and the dissolution rate is directly proportional to the current density [16]. In Fig. 2, the total amount of silicon removed (etch time)$\times$(current density)$=6000$ mC/cm^2, denoted as (Q), was held constant for all samples. Gravimetric analysis of the samples prepared under each condition gave similar mass loss values, leading us to believe that charge loss to the oxidation of the electrolyte is highly implausible. Samples prepared at twice the current density were, therefore, etched for half as long. Here we see that 'islands' are present in all samples, in contrast to previous work where these features were only observed at high current densities [10]. The sample in Fig. $2A_1$ was produced at a low current density ($J=5$ mA/cm^2), and exhibits a distinctive 'mesa' structure where the porous silicon network has collapsed laterally (in two dimensions parallel to the surface) leaving large visible cracks in the surface. The curling (three-dimensional collapse) observed at high current density as seen in Fig. $2C_1$, however, is not observed in this sample. At the base of the mesas, the PS–Si interface remains intact and the PS network has not collapsed appreciably in this region. The fluorescence from the low current density sample also indicates that the PS–Si interface remains intact. Fig. $2A_2$ shows a high-resolution fluorescence micrograph of a sample prepared at low current density. The top of each mesa shows nearly uniform luminescence with the only contrast occurring between the mesas and the cracks. While the scale for the image in Fig. $2A_2$ has been adjusted to enhance this contrast, the bottom of the crack regions are emitting at $\sim$25% the intensity of the tops of the mesas. This suggests that the PS framework remains attached to the silicon substrate at the PS–Si interface following evaporation-induced pore collapse. A representative luminescence spectrum of this sample is shown in Fig. $2A_3$. The spectrum is very broad and peaked in the red region of the visible spectrum. The width of the spectrum suggests a wide range of chromophore sizes, which is consistent with a slow etching process where the existing pores grow wider while the thickness of the PS layer grows deeper. It is important to note that there is very little spatial variation in the shape of the luminescence spectrum for this sample.

The collapsed 'mesa' features in the low current density samples have been attributed to differential lattice strain present between the top and bottom of the layer due to a decrease in the amount of silicon removed with increasing depth [17]. Others have attributed the initial shrinkage to a capillary pore mechanism during drying, which is later stabilized by van der Waals forces between adjacent pore walls. This work suggests that local variation in porosity result in dramatically increased ($\propto 1/$porosity) and asymmetric capillary forces which induce fracturing of the PS network [18]. Indeed, the large cracks visible in Fig. $2A_1$ may have been a result of these asymmetric forces. This seems to suggest that the pore structure within the mesas seen here, which appear free of cracks, is more or less uniform, with a gradual decrease in porosity (specifically pore size) with depth. In all samples produced at low current densities ($J<10$ mA/cm^2), the porous silicon network is relatively thick ($\sim$10 μm) and remains rigidly fixed to the Si substrate.

For samples etched at moderate current densities ($J=$ 8–12 mA/cm^2), the porous silicon network was somewhat thinner ($\sim$5 μm). During the drying process, cracks seem to be formed leaving 'platelets' of nearly uniform thickness which are only loosely bound to the substrate (see Fig. $2B_1$) and show a slight curling around their edges. If the current density is increased to $J>12$ mA/cm^2, an even higher degree of curling at the edges is observed and the overall film thickness is reduced. In addition, for these high current density samples, the thickness of the platelet varies across the platelet from only a few μm in the middle to $\sim$5 μm near their edges (Fig. $3C_1$). It is clear that samples produced at high current densities have a different collapsed morphology, and a subsequently different pore structure, than the low current density samples. In contrast to the low current density samples, the fluorescence micrographs of the moderate and high current density samples (Fig. $2B_2$ and C_2, respectively) exhibit cracks that are non-luminescent. In these regions, the PS network has broken free of the Si substrate during collapse, leaving bare non-luminescent Si. This curling and platelet formation, along with the decrease in film thickness, indicates etching and pore collapse in all three dimensions. Since the total charge and the total Si removed is constant for all three samples, the three-dimensional etching and collapse suggests that the pore size and the

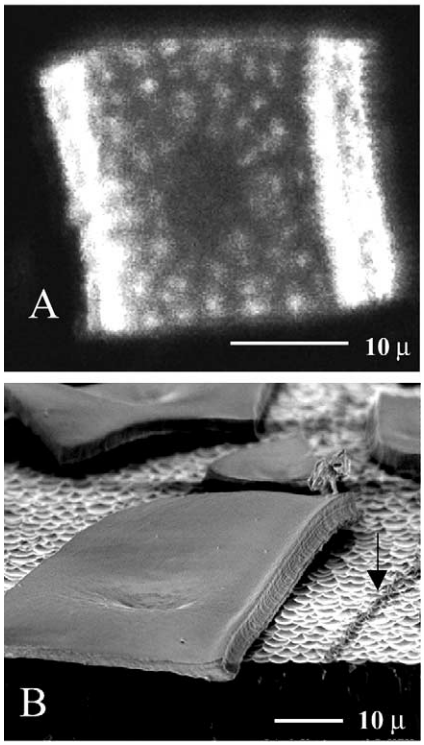

Fig. 3. Representative luminescence (A) and SEM micrographs (B) of a single platelet from a typical moderate current density sample (10 mA/cm^2). The brightest emission originates from the edge of the platelet while a dark region is clearly visible in the center. This dark region is attributed to the small dip, visible in (B), where the PS platelet remains attached to the Si substrate.

chromophore size decreases. In the context of the quantum confinement model, this would imply that the luminescence spectrum would blue-shift for the higher current density samples [19].

The moderate current density samples have a spectrum (Fig. 2B$_3$), slightly narrower and blue-shifted compared to the spectrum for the low current density sample (Fig. 2A$_3$). Here, the majority of the etching proceeds normal to the surface; however, some pores are formed laterally into the existing pore walls. As a result, the degree to which the existing pores are widened is reduced, and the distribution of chromophore sizes is somewhat smaller. At high current densities, the spectrum is quite narrow and dramatically blue-shifted (Fig. 2C$_3$), suggesting that the pores are not appreciably widened. Therefore, etching must proceed to a great extent laterally into the new pore walls throughout the etching process. The web-like pore network results in a much narrower distribution of chromophore sizes. The investigation of individual chromophores within single porous silicon nanoparticles is explained in detail in some of our recent work [20]. It is important to note that the green-emitting and blue-emitting PS samples produced in our lab all have the morphology of Fig. 2C$_1$. We have not been able to make green-emitting or blue-emitting PS with the morphology of Fig. 2A$_1$. This implies that there is a direct link between the pore size and the chromophore size. Furthermore, higher current density samples produce the smallest pores and the bluest emitters. Similar shifts in photoluminescence, due to the shrinking in size of the silicon core of silicon nanocrystals, have also been reported [21].

We have also observed other interesting features in the luminescence images of the higher current density samples. Running through the middle of the cracks between adjacent platelets is a very small fragmented line of porous silicon, which is only faintly visible in the fluorescence image (Fig. 2B$_2$ — black arrow), but is more notable in the electron micrograph (Fig. 3B — black arrow). Other groups have been observed these in SEM data, and we concluded that these are the remains of the most active etching regions [10]. This, however, seems unlikely considering our data, because these regions lie directly between adjacent platelets are highly aligned, emit with the same luminescence spectrum as the rest of the sample, and are only formed during drying and collapse. The regions of highest etching, on the other hand, should be more randomly distributed throughout the sample. It seems more likely that the cracks are formed at a region of high stress, possibly due to a lattice defect, and then propagate rapidly through the pore structure. The crack propagation progresses quickly and does not allow the PS–Si interface time to relax. The adjoining platelets then 'unzip' leaving the remains of their intersection, which are luminescent.

The micrographs of Fig. 2B$_2$ and C$_2$ show a non-uniformity in the emission of the platelets themselves. The edges of the platelets have a much higher emission intensity, as was also observed in Fig. 1. Also, there is a distinct dark spot in the center of each of the platelets of Fig. 2C$_2$. Fig. 3a shows a higher magnification luminescence image of one of these platelets. A SEM image of a similar platelet is shown in Fig. 3b. In the SEM image, it is clear that the edges of the platelet have lifted free of the Si substrate. The center of the platelet remains attached, however, as is evidenced by the small visible depression where the PS has collapsed downward to a greater extent than the rest of the platelet. The details of this collapse are discussed in greater detail later in this text. In the corresponding fluorescence image, the center of the platelet has a dark spot at the point where the PS is still attached to the substrate. For sufficiently thin samples, like those shown in Fig. 2, the optical exciton may only need to travel a few hundred nanometers through the PS framework into the Si substrate, where it can relax non-radiatively through an efficient phonon process.

In Fig. 4, the layer thickness vs. time for several current densities are plotted. Unfortunately, as the current density is increased, the total time at which a sample

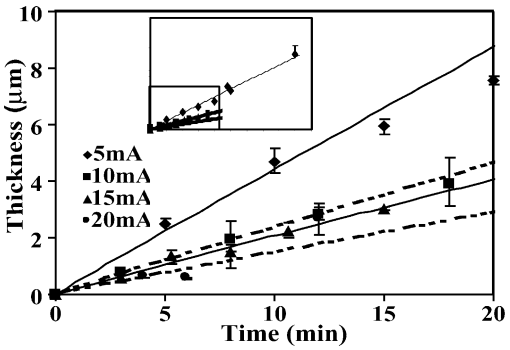

Fig. 4. Sample thickness plotted as a function of time for samples etched at various current densities denoted in the legend. The solid lines represent linear fits to each data set. The slopes for the 5, 10, 15 and 20 mA/cm^2 samples are 0.46, 0.25, 0.22 and 0.16, respectively. The inset shows the entire data set for the low current density (5 mA/cm^2) sample, which includes etch times of 24, 25 and 45 min. The higher current density samples could not be etched for this long due to electro-polishing of the Si surface.

can be etched before electro-polishing occurs, or fatal damage at the PS–Si interface, decreases dramatically. This decreases the total range of current densities possible; however, the available data still provide a qualitative understanding of the etching process. We can see that, for the low current density case, the thickness of the PS layer increases at a rate of $\sim$1 μm per min. When the current density is increased by at least a factor of two ($J>10$ mA/cm^2), the etching rate into the Si substrate is decreased by approximately the same factor. Again, this suggests that at low current densities a two-dimensional etching mechanism dominates on this time scale, while at higher current densities, a three-dimensional process seems to dominate. These data, however, do not provide a specific insight into the geometry of the pore network. For example, we cannot determine whether the pores are widening during the three-dimensional etching, or if secondary pores are nucleating laterally into the walls of existing pores. It is this level of detail that will help us to understand the potential distribution of pore sizes, and more importantly, chromophore sizes within the sample and how they depend upon etch conditions.

In order to effectively determine the relationship between etch conditions and pore morphology, groups of samples were prepared, in which the total charge, and hence the total amount of silicon removed, was held fixed. The plots in Fig. 5 represent two such groups, having (current density)$\times$(etch time), or Q values of 4800 and 7200, respectively. Each point in this plot represents the average porous silicon thickness obtained from 8 to 10 regions on each of 3–5 reproduced samples for each set of conditions. All measurements were taken edge-on at the thinnest point along each platelet or mesa structure and exhibit several interesting features. First, at low current density ($J<10$ mA/cm^2), the thickness is strongly dependent on the current density. While at higher current densities ($J>10$ mA/cm^2), the thickness is only weakly dependent on the rate at which charge is injected into the sample. Secondly, at low current densities the thickness scales nearly proportionally with the amount of silicon removed, but at higher current densities the thickness approaches a similar asymptotic value regardless of the total charge (Q) used. This supports the conclusion that, at a low current density, the pores are formed normal to the Si substrate and the pore depth is a nearly linear function of the etch time. For higher current density samples, where the same amount of Si has been removed, etching must proceed both normal to the surface as well as laterally into the walls of the newly formed pores.

Now that we have established a connection between bulk morphology and pore geometry for samples prepared under different etching conditions, we can begin to outline a model. In the case of the low current density samples, the injected charge moving up through the Si substrate has sufficient time to reorganize around local surface state minima. Electrochemical etching begins at these points of higher charge density, resulting in the removal of material, which in turn creates new energy minima at the bottom of the newly formed pits, awaiting the arrival of the next set of injected charges (Fig. 6A,B) [11]. This process is continuous and the resultant cylindrical pores are formed more or less normal to the silicon substrate. For the high current density samples, however, the process is significantly different. Here, the initial charge density is sufficient to begin etching before charge migration to surface minima can occur, resulting in a large number of inhomogeneous pores (Fig. 6E). Likewise, subsequent charges need only reach the Si–electrolyte interface to induce etching. In this manner, the pore structure forms laterally into the walls of the

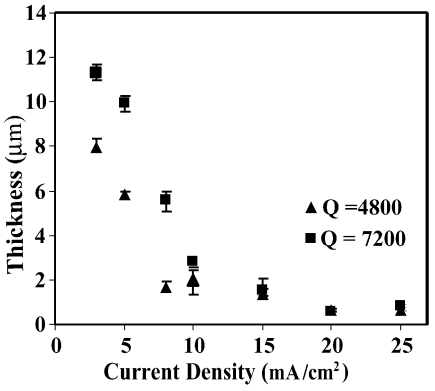

Fig. 5. Thickness as a function of etching time for $Q=4800$ and 7200 mC/cm^2, respectively. Each point represents an average thickness measured for >10 platelets and the error bars represent the entire range. The two curves converge at a current density of $\sim$15 mA/cm^2.

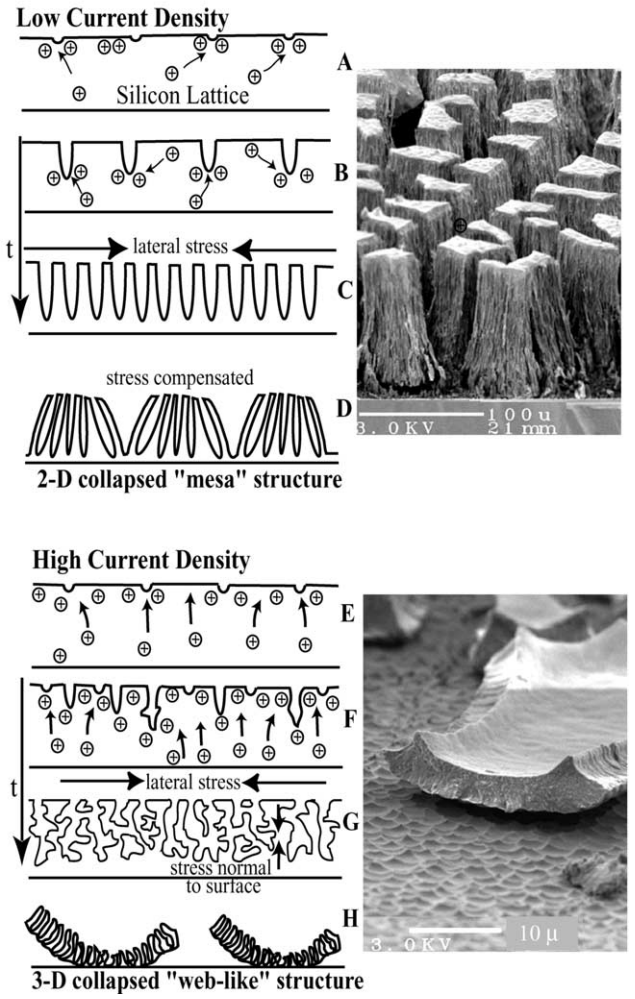

Fig. 6. Pore formation and evaporation induced collapse model for low (pictures A, B, C and D) and high (pictures E, F, G and H) current density samples with representative SEM images (right). At low current density injected holes reorganize around surface minima (shown in A) and pores continually form normal to the surface (shown in B). During drying, the pore structure experiences strong lateral capillary forces (C), which are compensated by pore collapse, parallel to the Si substrate, and the subsequent formation of mesa-like structures (shown in D). At high current density, the dissolution valence of Si is satisfied prior to carrier reorganization (shown in E), resulting in random and rapid pore formation (F). The resulting sponge-like pore structure is stressed both laterally and normal to the Si substrate by evaporation induced capillary forces during drying (shown in G). The web-like Si lattice collapses three-dimensionally and non-uniformly, partially fracturing the PS–Si interface, and resulting in the formation of curled platelets (shown in H). Thickness and chromophore sizes are not drawn to scale.

initial pores, as well as normal to the substrate (Fig. 6F). The resulting highly porous silicon network is analogous to a 'sponge' with a large number of interconnecting pores. This 'web-like' structure has been directly observed by others using high resolution TEM [9].

As material is removed in the electrochemical process, breaking up of the Si–Si framework at the pore interface results in an increase in the lattice parameter relative to the bulk (compression). During drying, when liquid evaporates from the highly porous network, surface tension overwhelms the porous network, causing it to collapse. As air replaces the liquid inside each pore, surface tension at the air–liquid interface strongly pulls the sides of the pores together and the porous network shrinks. As drying proceeds, the network continues to collapse, resulting in a decrease in porosity. The maximum pressure exerted on the pore walls is given by the Laplace equation:

$$\Delta P = -2\gamma/r \quad (1)$$

where r is the radius of the pore, and γ is the surface tension of the electrolyte ($\sim$22 mJ m^{-2} for ethanol). We can now apply this to our simple structural model.

Samples prepared at low current densities have a large average pore diameter, resulting in relatively small pressures during evaporation. The surface-induced stress exists primarily laterally between the wall of the pores due to the orientation of cylindrical pores normal to the surface (Fig. 6C). The size of the Si lattice is sufficient to endure the induced lateral stress without fracturing at the Si–PS interface; therefore, the surface of the pores collapse to a greater extent. The collapsed structures resemble 'mesas', which are stabilized by the strong van der Waals forces between the opposing pore walls (Fig. 6D).

For high current density samples, the pore radii are much smaller, resulting in larger pore pressures. In addition, the quantity of silicon within the lattice, relative to these forces, is insufficient to prevent fracturing at the Si–PS interface. The web-like or sponge-like pore geometry suggests that opposing pore walls will exist in all three dimensions (Fig. 6G). The stress experienced by the lattice will, therefore, be both lateral and normal to the Si substrate. The lateral stress, which is first felt at the surface of the layer, decreases with depth and causes the surface to contract more relative to the bottom of the layer. The PS–silicon layer begins to fracture at a point where the pressure relative to the strength of the Si framework is greatest, and propagates rapidly forming the edge of the platelet. The pressure gradient across the platelet causes the lattice to curl away from the substrate (Fig. 6H). The pores collapsing normal to the surface contribute to the lateral collapse of the platelet, as well as decreasing the thickness of the PS layer.

4. Conclusions

Rapidly dried porous silicon samples produced under varying etch parameters, but with the same pore volume, exhibit a range of collapse-induced morphologies. While all samples appear to form island structures during collapse, there are two distinct morphology classes: relatively tall pillars formed at low current densities;

and thin curled platelets formed at higher current densities.

The observed morphology in these samples depends much less on the total void space (porosity) than on the applied current density during etching. At low current density ($J<10$ mA cm^2), cylindrical pores are formed which collapse two-dimensionally (laterally) during drying. These pores widen as function of etch time and result in a broad distribution of chromophore sizes, observed as a very broad fluorescence emission lineshape. Higher current density samples ($J>10$ mA/cm^2) collapse three-dimensionally suggesting an interconnecting network of pores. This network of pores may be highly non-periodic; however, the Si chromophores produced are much smaller and have a much narrower distribution of sizes, which results in the narrow blue-shifted fluorescence emission profile compared to the low current density samples.

References

[1] L.T. Canham, Appl. Phys. Lett. 57 (1990) 1046.
[2] A.G. Cullis, L.T. Canham, P.D.J. Calcott, Appl. Phys. Lett. 82 (1997) 909.
[3] V. Lehmann, U. Go sele, Appl. Phys. Lett. 58 (1991) 856.
[4] N. Ookubo, T. Matsuda, Y. Ochiai, N. Kuroda, Mater. Sci. Eng. B20 (1993) 324.
[5] D. Brumbead, L.T. Canham, D.M. Seekings, P.J. Tufton, Electrochim. Acta 38 (1993) 191.
[6] E. Muhlen, D. Zur, S. Chang, S. Rogaschewski, H. Niehus, Physica Status Solidi (b) 198 (1996) 673.
[7] L.N. Aleksandrov, P.L. Novikov, Thin Solid Films 330 (1998) 102.
[8] V. Parkhutik, Solid-State Electron. 43 (1999) 1121.
[9] S. Li, S. Silvers, J.M.S. El-Shall, J. Phys. Chem. B101 (1997) 1794.
[10] C.-R. Lin, S.-C. Lee, Y.-R. Chen, J. Appl. Phys. 75 (1994) 7728.
[11] O. Teschke, Appl. Phys. Lett. 64 (1994) 1986.
[12] M.J. Sailor, E.J. Lee, Adv. Mater. 9 (1997) 783.
[13] K.D. Weston, S.K. Buratto, J. Phys. Chem. A 102 (1998) 3635.
[14] N. Noguchi, I. Suemune, M. Yamanishi, G.C. Hua, N. Otsuka, Jpn. J. Appl. Phys. 31 (1992) 490.
[15] J.M. Lauerhaas, G.M. Credo, J.L. Heinrich, M.J. Sailor, J. Am. Chem. Soc. 114 (1992) 1911.
[16] Y. Seo, Hun, K. Nahm, Suk, M. An, Hwan, E.K. Suh, Y. Lee, Hee, K. Lee, Bang, H. Lee, Jae, Jpn. J. Appl. Phys. 33 (1) (1994) 6425.
[17] S.D. Campbell, L.A. Jones, E. Nakamichi, R.-X. Wei, L.D. Zajchowski, J. Vacuum Sci. Technol. 13 (1995) 1184.
[18] U. Gruning, A. Yelon, Thin Solid Films 255 (1995) 135.
[19] M.V. Wolkin, J. Jorne, P.M. Fauchet, G. Allan, C. Delerue, Phys. Rev. Lett. 82 (1999) 197.
[20] M.D. Mason, D.J. Sirbuly, P.J. Carson, S.K. Buratto, J. Chem. Phys. 114 (2001) 8119.
[21] J.A. Carlisle, M. Dongol, I.N. Germanenko, Y.B. Pithawalla, M.S. El-Shall, Chem. Phys. Lett. 326 (2000) 335.